Nussbaum for skillful technical assistance.

Registry No. PheRS, 9055-66-7; Lys, 56-87-1.

REFERENCES

Baltzinger, M., Fasiolo, F., & Rêmy, P. (1979) *Eur. J. Biochem. 97*, 481-494.

Beauvallet, C., Hountondji, C., & Schmitter, J. M. (1988) *J. Chromatogr. 438*, 347-357.

Bedouelle, H., & Winter, G. (1986) *Nature 320*, 371-373.

Brunie, S., Mellot, P., Zelwer, C., Risler, J. L., Blanquet, S., & Fayat, G. (1987) *J. Mol. Graph. 5*, 18-21.

Ducruix, A., Hounwanou, N., Reinbolt, J., Boulanger, Y., & Blanquet, S. (1983) *Biochim. Biophys. Acta 741*, 244-250.

Fayat, G., Hountondji, C., & Blanquet, S. (1979) *Eur. J. Biochem. 96*, 87-92.

Fersht, A. (1985) *Enzyme Structure and Mechanisms*, Freeman, New-York.

Hill, K., & Schimmel, P. (1989) *Biochemistry 28*, 2577-2586.

Hountondji, C., Fayat, G., & Blanquet, S. (1979) *Eur. J. Biochem. 102*, 247-250.

Hountondji, C., Blanquet, S., & Lederer, F. (1985) *Biochemistry 24*, 1175-1180.

Hountondji, C., Lederer, F., Dessen, P., & Blanquet, S. (1986a) *Biochemistry 25*, 16-21.

Hountondji, C., Dessen, P., & Blanquet, S. (1986b) *Biochimie 68*, 1071-1078.

Hountondji, C., Schmitter, J. M., Beauvallet, C., & Blanquet, S. (1987) *Biochemistry 26*, 5433-5439.

Labouze, E., & Bedouelle, H. (1989) *J. Mol. Biol. 205*, 729-735.

Laemmli, U. K. (1970) *Nature 227*, 680-685.

Mechulam, Y., Dardel, F., Le Corre, D., Blanquet, S., & Fayat, G. (1990) *J. Mol. Biol.* (in press).

Merrifield, R. B. (1963) *J. Am. Chem. Soc. 85*, 2149-2153.

Muller, S., Himmelspach, K., & Van Regenmortel, M. H. V. (1982) *EMBO J. 1*, 421-425.

Raffin, J. P., & Rêmy, P. (1978) *Biochim. Biophys. Acta 520*, 164-174.

Renaud, M., Fasiolo, F., Baltzinger, M., Boulanger, Y., & Remy, P. (1982) *Eur. J. Biochem. 123*, 267-274.

Roques, P., Thomê, F., Dubord, C., & Olomucki, M. (1989) *Biochim. Biophys. Acta 1009*, 99-102.

Rould, M. A., Perona, J. J., Söll, D., & Steitz, T. A. (1989) *Science 246*, 1135-1142.

Sampson, J. R., Rihenzo, A. B., Behlen, L. S., & Uhlenbeck, O. C. (1989) *Science 243*, 1366.

Sanger, F., Nicklen, S., & Coulson, A. R. (1977) *Proc. Natl. Acad. Sci. U.S.A. 74*, 5436-5467.

Sanni, A., Mirande, M., Ebel, J. P., Waller, J. P., & Fasiolo, F. (1988) *J. Biol. Chem. 263*, 15407-15415.

Sanni, A., Walter, P., Ebel, J. P., & Fasiolo, F. (1990) *Nucleic Acids Res. 18*, 2087-2092.

Sayers, J. R., Schmidt, W., & Eckstein, F. (1988) *Nucleic Acids Res. 16*, 791-802.

Kinetics and Mechanism of the Pressure-Induced Lamellar Order/Disorder Transition in Phosphatidylethanolamine: A Time-Resolved X-ray Diffraction Study[†]

Andrês P. Mencke and Martin Caffrey*
Department of Chemistry, The Ohio State University, Columbus, Ohio 43210-1173

Received February 8, 1990; Revised Manuscript Received October 29, 1990

ABSTRACT: By using synchrotron radiation, a movie was made of the X-ray scattering pattern from a biological liquid crystal undergoing a phase transition induced by a pressure jump. The system studied includes the fully hydrated phospholipid dihexadecylphosphatidylethanolamine in the lamellar gel ($L_{\beta'}$) phase at a temperature of 68 °C and a pressure of 9.7 MPa (1400 psig). Following the rapid release of pressure to atmospheric the $L_{\beta'}$ phase transforms slowly into the lamellar liquid crystal (L_α) phase. The pressure perturbation is applied with the intention of producing a sudden phase disequilibrium followed by monitoring the system as it relaxes to its new equilibrium condition. Remarkably, the proportion of sample in the L_α phase grows linearly with time, taking 37 s to totally consume the $L_{\beta'}$ phase. The time dependencies of radius, peak intensity, and width of the powder diffraction ring of the low-angle (001) lamellar reflections were obtained from the movie by image processing. The concept of an "effective pressure" is introduced to account for the temperature variations that accompany the phase transition and to establish that the observed large transit time is indeed intrinsic to the sample and not due to heat exchange with the environment. The reverse transformation, L_α to $L_{\beta'}$, induced by a sudden jump from atmospheric pressure to 9.7 MPa, is complete in less than 13 s. These measurements represent a new approach for studying the kinetics of lipid phase transitions and for gaining insights into the mechanism of the lamellar order/disorder transition.

A fundamental characteristic of a lipid phase transition is its intrinsic transit time, the shortest possible time in which the sample can completely transform from one phase to another. To tackle the problem of measuring the transit time, various temperature-jump methods have been used in which a high-energy pulse is applied to a sample with the intent of instantaneously and uniformly raising its temperature by a measurable amount, ΔT, aiming to render the initial phase unstable and observing its relaxation to the new equilibrium condition. Achieving a rapid, uniform, and nondestructive increase in temperature in a controlled and reproducible

---

[†] This work was supported by a grant from the National Institutes of Health (DK36849), a University Exploratory Research Program Award (The Procter and Gamble Co.), and a Du Pont Young Faculty Award to M.C.

manner in hydrated lipid samples is difficult in practice regardless of whether the energy pulse derives from an electric current (Tate, 1988), a hot fluid stream (Caffrey, 1985, 1987), microwaves (Caffrey, 1990a,b), or laser light (Kriechbaum et al., 1989). Furthermore, rapid cooling is considerably more difficult to obtain than rapid heating. In contrast, a change in pressure, just as important as temperature in defining the thermodynamic state of the system, is much more rapidly and uniformly distributed throughout the sample. Moreover, a pressure jump has the advantage of being bidirectional. Obtaining useful pressure-jump data requires a greater investment in experimental equipment and technique than temperature jumps, so that the field of pressure-jump studies on biological materials is still relatively uncharted.

As with other relaxation methods, pressure-jump measurements are not without difficulties. For example, changes in pressure couple into temperature changes via the heat of the transition (ΔH), the work ($P\Delta V$) done on the lipid, and the dissipation due to friction. Le Chatelier's principle is at work here, and this pressure–temperature coupling tends to counter the effect of the pressure jump. However, in-sample temperature can be measured during the experiment and the system can be described in terms of the combined pressure–temperature perturbation.

The time evolution of the X-ray scattering pattern during a pressure-jump-induced phase transition in a lipid is presented here for the first time. On the basis of these measurements, the kinetics of the lamellar chain melting transition has been established and insights into the mechanism of this order/disorder transition have been obtained. Such information is integral to our understanding of the nature of lipid phase transitions that occur in biological, model, and reconstituted membranes and in formulated systems.

EXPERIMENTAL PROCEDURES

Materials. DHPE,[1] obtained from Fluka Chemical Corp. (Hauppage, NY), was used as purchased and without further purification. Purity has been reported on previously (Caffrey, 1985). Water was obtained from a Milli-Q water purification system (Millipore). All other chemicals and solvents were of reagent grade.

Sample Preparation. Fully hydrated samples of DHPE were prepared for X-ray diffraction measurements as previously described (Caffrey, 1985). Although always fully hydrated, the samples had a pastelike consistency.

X-ray Diffraction. (*A*) *X-ray Source and Camera.* Measurements were made by using wiggler-enhanced, monochromatic (0.1564 nm), focused X-rays on the A1 line at the Cornell High-Energy Synchrotron Source (CHESS) as previously described (Caffrey, 1987) with the following modifications. A 10-cm-long cylindrically bent asymmetric crystal of germanium (111) was used for monochromatization and horizontal focusing. Higher order harmonics were eliminated and the beam was vertically focused by using a 60-cm-long platinum- or nickel-coated mirror. Beam size at the collimator was (nominally) 1.5 mm wide and 0.3 mm high, providing 5.1×10^{10} photon/s down at 0.3-mm-diameter collimator (Supper) with the storage ring operating at 5.44 GeV and 53 mA total electron beam current.

X-radiation damage was kept to a minimum by taking the precautions outlined earlier (Caffrey, 1984, 1987). At no point in the course of these measurements was any one part of the sample exposed to the beam for longer than 1 min.

Static and time-resolved X-ray diffraction (TRXRD) measurements were made by using a home-built low-angle X-ray diffraction camera with a 0.3-mm-diameter collimator as described earlier (Caffrey, 1987) with the following modification. Instead of lens coupling, the image intensifier was coupled via a reducing fiber optic (Gallileo) to the fiber-optic faceplate on the front surface of a CCD video camera (Model 3000F, Fairchild). The demagnification of the reducing fiber optic is 2.27:1, and the CCD itself measures 14.4 mm diagonally with a vertical/horizontal aspect ratio of 3/4 and a resolution of 488 vertical by 380 horizontal picture elements (pixels). To minimize distortion, measurements were confined to the area of a circle, 20 mm in diameter, positioned at the center of the front face of the image intensifier.

(*B*) *Static X-ray Diffraction.* X-ray sensitive film (DEF5, Kodak, Rochester, NY) was used to record diffraction patterns. Sample temperature was controlled by using a forced-air crystal heating/cooling apparatus (Model XR-85-1, FTS Systems, Inc., Stone Ridge, NY) as previously described (Caffrey, 1987). Temperature stability during a given measurement is estimated to be ~±0.5 °C. Accuracy is no better than ±1.5 °C. X-ray wavelength was determined by using a lead nitrate standard and a carefully measured sample-to-film distance (Caffrey, 1987).

(*C*) *Time-Resolved X-ray Diffraction.* The essential components of the system used to make TRXRD measurements include a two-dimensional, live-time X-ray imaging device, a character generator interfaced to a digital voltmeter (thermometer), an electronic clock, a video camera, recorder, and monitor, and an image processor. These, along with their performance characteristics, have been described earlier (Caffrey, 1987).

Pressure Jump. (*A*) *The Pressure Cell.* Quartz X-ray capillaries of nominally 0.7-mm diameter and 10-μm wall thickness (Supper) were used as pressure cells capable of supporting maximum pressures from 10 to 20 MPa before rupture. There was some variation in the dimensions of individual capillaries from a given batch. Generally, capillaries with smaller diameters withstood the highest pressures.

Continuous in-sample temperature readings were provided by a Teflon-coated copper–constantan thermocouple (the junction itself was exposed to the lipid) of 0.003-in. diameter (Omega). The feed-through for the wires consisted of a Vespel ferrule (Alltech) seated in a Swagelock fitting. A drop of Surehold glue was used as a sealant (Figure 1).

Pressure was applied to the cell by connecting it, by means of Swagelock pipe fittings, stainless steel and Flexon tubing (Alltech), and hand-operated valves (Parker), to the output of a high-pressure regulator (maximum output pressure 2000

---

[1] Abbreviations: A_0 and A, maximum and instantaneous peak area, respectively; CCD, charge-coupled device; CHESS, Cornell High-Energy Synchrotron Source; $\mathbf{d}$, lamellar repeat vector; d, interlamellar spacing; DHPE, dihexadecylphosphatidylethanolamine; DSC, differential scanning calorimetry; f, relative fraction; hwhm, half-width at half-maximum; $I(S)$, the total scattering from a coherently scattering stack of lamellae; $I_u(S)$, scattering intensity from a single lamellar repeat unit; $\mathbf{k}$ and $\mathbf{k}'$, incident and scattered wave vectors, respectively; L_α, lamellar liquid crystal phase [the lipid phase notation used is that of Luzzati (1968)]; L_β, lamellar gel phase; M, maximum intensity or peak height; N, number of lamellae in a coherently diffracting domain; μ, peak position (Å^{-1}); P, pressure; P_t, transition pressure; P^*, effective pressure; $\mathbf{S} = (\mathbf{k}'/\mathbf{k})/(2\pi) = (2 \sin \theta)/\lambda$, scattering vector; $\mathbf{S}_M$, scattering vector at which the scattering intensity reaches its peak value; ΔS, theoretical full-width at half-height; σ, experimental peak half-width at half-height; s, half-width due to finite size effect; T, temperature; T_t, transition temperature; TRXRD, time-resolved X-ray diffraction; 2θ, scattering angle; U, internal volume; ΔH, enthalpy change; ΔV, volume change; x, distance along radius from diffraction pattern center; Δx, resolution of CCD and image processor; r^2, correlation coefficient.

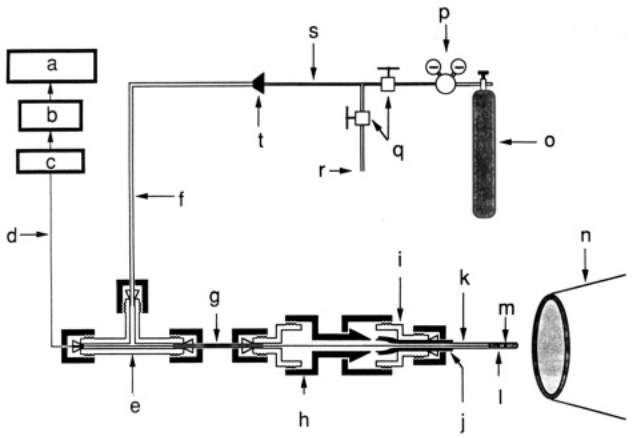

FIGURE 1: Schematic of the pressure cell and associated plumbing used in kinetic TRXRD studies of the pressure-jump-induced lamellar phase transition in hydrated DHPE. (a) Videocassette recorder; (b) character inserter; (c) voltmeter; (d) plastic coated thermocouple wire; (e) T-junction adapter; (f) Flexon tubing ($^1/_{16}$-in. o.d., 0.007-in. i.d.); (g) $^1/_{16}$-in. steel tubing; (h) tube adapter; (i) $^1/_4$–$^1/_{16}$-in. reducing union; (j) Teflon tubing; (k) X-ray capillary; (l) thermocouple junction; (m) X-ray beam; (n) forced-air crystal heater/cooler; (o) argon cylinder (2640 psi, 18.2 MPa, 180 atm); (p) high-pressure regulator; (q) valves; (r) outlet to atmosphere; (s) $^1/_4$-in. steel tubing; (t) adapter.

psig, 140 bar, 14 MPa) on a commercial argon gas cylinder.

The quartz capillary was connected to a $^1/_{16}$-in. female "T" (Swagelock) by means of a polyimide ferrule (Alltech) with a $^1/_{16}$-in. hole. A small section of 0.4-mm-diameter Teflon tubing was widened with a needle and used as a sleeve to protect the quartz capillary from direct contact with the polyimide ferrule, reducing the stress concentrations on the capillary during fitting. The pressure jump was obtained by rapidly opening appropriate hand-operated valves. Because the argon gas must flow through a narrow (0.004-in. i.d.) 20-cm-long Flexon tube, the pressure took up to 2 s to equilibrate.

(*B*) *Measurement of Pressure*. Equilibrium pressure values were obtained from a Bourdon gauge at the outlet of the high-pressure regulator.

The time evolution of pressure during the pressure jump was obtained subsequently and separately from the TRXRD and temperature measurements as follows. A pressure transducer of known volume was connected in place of the assembly containing the quartz capillary and thermocouple feed-through, and the pressure was recorded as a function of time. The pressure rise and decay curves were then corrected for the difference in volumes of the transducer and the assembly (Appendix). This procedure is valid because (a) the pressure gradients in the assembly and in the lipid are negligible and (b) the lipid is essentially incompressible (Cevc & Marsh, 1987) and occupies only a very small fraction of the total volume of the assembly, so that the presence or absence of lipid does not affect the pressure.

Data Analysis. (*A*) *Nonlinear Least-Squares Modeling of the Diffraction Data*. Our raw data consist of two-dimensional, powder diffraction patterns, or parts thereof, recorded in live time at video frame rates (30 frames/s) on videotape. Image processing (Recognition Concepts Inc., Trapix 55/48 hardware; Tau Corp., RTIPS software) enables us to grab and to digitize individual frames as necessary (our typical sampling rate is ca. 10 frames/s), which are analyzed in the following way. The center and radius of a software-produced image of a circle are overlaid onto the powder diffraction ring of interest and its center and radius are varied interactively until the circle matches up with the powder ring, thus determining a center and radius for the diffraction ring. Subsequently, an intensity scan as a function of distance from the center is obtained by averaging the intensities over a 20° arc centered on the vertical diameter of the ring. The purpose of averaging is to enhance the signal-to-noise ratio in the final intensity as a function of radius ($I - 2\theta$) scan. Averaging over larger angles up to 360° is sometimes possible but in most cases is limited by image distortions introduced in the intensifier/camera system (Caffrey & Bilderback, 1984). To prevent distortions from introducing errors, the arc is chosen to be 20°, a size for which deviation of the diffraction rings from perfect circularity is insignificant. The annular sector utilized in the averaging has inner and outer radii of 110 and 212 pixels, respectively, and contains the entire spread in the radii of the diffraction rings throughout the pressure-jump experiment.

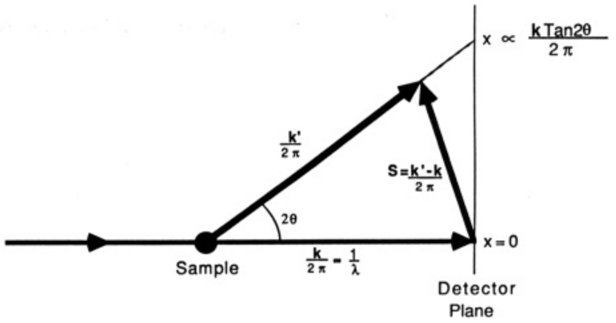

FIGURE 2: Low-angle X-ray scattering geometry. At low angles the following approximations hold: 2θ (radians $\approx \tan 2\theta \approx \sin 2\theta$. We also note that $|\mathbf{S}| = S = (k \sin \theta)/\pi = (2 \sin \theta)/\lambda$ and thus $x \propto 2\theta/\lambda \approx S$.

During the phase transition, when two phases are present, the $I - 2\theta$ scan has the appearance of a double-peaked function of the radius with each peak arising from a separate phase [see Figure 5 in Caffrey (1985)]. To characterize the $I - 2\theta$ scan, the experimentally determined function is fitted by a nonlinear least-squares method (Press et al., 1986) to the model function

$$f_{\mathrm{fit}}(x;M_\alpha,\mu_\alpha,\sigma_\alpha,M_{\beta'},\mu_{\beta'},\sigma_{\beta'},C) = \frac{M_\alpha}{1 + \left(\dfrac{x - \mu_\alpha}{\sigma_\alpha}\right)^2} + \frac{M_{\beta'}}{1 + \left(\dfrac{x - \mu_{\beta'}}{\sigma_{\beta'}}\right)^2} + C \quad (1)$$

where M, μ, and σ are the maximum or peak height, the radial position, and the half-width at half-maximum of the peak, respectively, C represents the flat-field and background noise, x is the distance along the radius from the pattern center, and the indices α and β' refer to the L_α and $L_{\beta'}$ phases, respectively. [Referring to Figure 2, we have $x = (\tan 2\theta)/\lambda \approx 2\theta/\lambda$, where x is given in reciprocal angstroms when θ is in radians and λ is the X-ray wavelength in angstroms.] The values of the parameters (M_α, μ_α, σ_α, $M_{\beta'}$, $\mu_{\beta'}$, $\sigma_{\beta'}$, and C) are determined as a function of time by sampling at the rate of ca. 10 frames/s. At any given time and radius, the deviation of f_{fit} from the data is typically within 3% or less. Assuming negligible distortion in the small region containing the two peaks, the photographic data in Table I are used to determine that, in this region, a deviation of 1 video pixel width corresponds to 1.23×10^{-4} Å^{-1}. The parameter C remains nearly constant throughout the experiment. Lorenz and polarization corrections were omitted since μ_α and $\mu_{\beta'}$ remain nearly constant, restricting the observations to the small separate portions of reciprocal space occupied by the (001) reflections in each of the two phases. If a larger region of reciprocal space is to be examined the intensities must be multiplied by x^2 (Lorenz correction) and divided by $(1 + \cos^2 2\theta)/2$ [polarization

Table I: X-ray Diffraction Data and Phase Designation for Hydrated Dihexadecylphosphatidylethanolamine: Dependence on Pressure and Temperature

pressure (psi)	0	0	0	500	800	1200	1600	2000
temperature (°C)	28	69	69	69	69	69	69	69
low-angle scattering (Å)	62.6	60.2		58.7	59.6	60.6	60.6	60.6
		52.7	52.9	52.9	52.9	52.9	52.9	52.9
	15.4	14.9		15.1	15.1	15.1	15.0	15.1
	12.4	13.1	13.1	13.2	13.2			
	10.3			9.97	10.0			10.1
wide-angle scattering[a] (Å)	4.13	4.30	D4.45	4.33	4.33	4.30	4.30	4.31
phase designation[b]	$L_{\beta'}$	$L_{\beta'}/L_\alpha$	L_α	$L_{\beta'}/L_\alpha$	$L_{\beta'}/L_\alpha$	$L_{\beta'}/L_\alpha$	$L_{\beta'}/L_\alpha$	$L_{\beta'}/L_\alpha$

[a] D denotes that the peak is diffuse; all others are sharp. In the case of phase coexistence, the center of the diffuse wide-angle peak is difficult to locate and is not reported. [b] Phase coexistence is indicated by $L_{\beta'}/L_\alpha$. Note that, under the conditions of these static diffraction measurements, transformation to the $L_{\beta'}$ phase at high pressure was incomplete, as evidenced by the presence of a trace of the (001) low-angle reflection in the pattern.

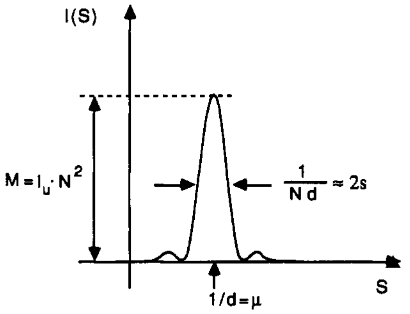

FIGURE 3: Schematic representation of the low-angle scattering peak and the experimentally measured quantities: maximum peak intensity (M), peak position (μ), and half-width at half-height (s). The plotted function shows the total scattering intensity $I(S)$ of a stack of N lamellae separated by a lamellar repeat distance d, each lamella possessing scattering intensity I_u.

correction; see Franks and Levine (1981)].

(*B*) *Low-Angle X-ray Scattering Theory.* We refer to the low-angle X-ray scattering geometry depicted in Figure 2. A more thorough description of X-ray scattering from lipid bilayers is given in Blaurock (1982) and Franks and Levine (1981). We have that the scattering intensity of the (001) lamellar reflection from a stack of N identical lamellae can be written as

$$I(S) = I_u(S)N^2\left|\frac{\sin(\pi NSd)}{N\sin(\pi Sd)}\right|^2 \quad (2)$$

where S is the component of the scattering vector in the direction of the bilayer normal, d is the lamellar repeat spacing, N is the number of lamellae, and $I_u(S)$ is the scattering intensity of one lamellar repeat unit. This formula has the following features, which can be related to the experimental $I - 2\theta$ scans as indicated in Figure 3:

(I) maximum intensity (or peak height) $I_u(S_M)N^2 = M$ (3)

(II) peak position located at $Sd = 1$ or $S_M = 1/d = \mu$ (4)

(III) approximate width of the peak $\Delta S = 2s \approx 1/Nd$ (5)

where s is the half-width. More exactly, Guinier (1963) gives $0.9/Nd$ for the full width at half-maximum and $1/Nd$ for the integral width. (The integral width is defined as the width of a rectangle of same height as the peak maximum and same area as the area under the peak). These quantities are based on an idealized, perfectly regular model and are not directly observed in the experiment but are subject to distortion, nonlinearities, and broadening due to the instrumental effects and irregularities of the sample proper, such as nonuniformity of interlamellar spacings. The observed half-width (σ) is thus not equal to s. As will be seen below, s can be obtained by correcting for broadening effects. The quantity Nd corresponds to the extent of the coherently reflecting domain in the direction of the bilayer normal and is called the *size* in this direction. It is equal to the sum of the N successive interlamellar distances (d) that constitute a coherently reflecting domain. Because the denominator of eq 5 contains the quantity Nd, we shall call s the half-width due to the size effect.

By means of image processing and the data analysis procedures outlined above, the experimentally observed quantities are obtained as a function of time for each of the two phases from the fit of the data to f_{fit}. They yield the following derived quantities:

(*IV*) *Relative Number of Lipid Molecules in Each Phase.* The area under the measured intensity scan is proportional to the amount of material giving rise to the diffraction peak [see Klug and Alexander (1974)]. If there are two phases present there will be two peaks, typically at different positions, each peak corresponding to a given phase. From the fitted peak height and width, the areas, A_α and $A_{\beta'}$, and the corresponding area fraction, $f_{\alpha,\beta'} = A_{\alpha,\beta'}/(A_\alpha + A_{\beta'})$, of each of the two phases, L_α and $L_{\beta'}$, can be determined. The interpretation of this area fraction as a measure of the relative amount of material in each phase is valid only if the sampling of the geometrically corrected structure factor remains constant during the transition.

(*V*) *Domain Size in the Direction of the Bilayer Normal* (*Given in Number* of *Lamellae, N*):

$$N = \mu/2s \quad (6)$$

where the half-width due to the size effect (s) is obtained from the observed peak half-width (σ) by correcting for instrumental and disorder broadening. Equation 6 is obtained from eqs 4 and 5.

On the Interpretation of Peak Width. As stated above and as discussed by Blaurock (1982), effects due to disorder and instrumentation affect the observed width of the diffraction peak such that it can no longer be identified directly with the size effect. The application of eq 6 thus hinges upon correct assessment of the contribution of the size effect to the observed width. Deviations from the orderly periodic arrangement of the scattering atoms reduce the coherence of the diffracted radiation causing disorder broadening of the diffraction peak. In the case of random disorderly deviations from the lamellar arrangement, this broadening is proportional to the square of the order of the the lamellar reflection (Guinier, 1963). Instrumental broadening is caused chiefly by the finite dimensions of the beam (Blaurock, 1982). We see from the data given under X-ray Diffraction that one vertical pixel corresponds to (14.4)(3/5)(2.72/488) = 0.048 mm. Thus, the (nominal) beam hwhm of 0.15 mm projected onto the detector corresponds approximately to 0.15/0.048 = 3.1 pixels or (3.1)(1.23)(10^{-4}) Å^{-1} = 3.8×10^{-4} Å^{-1}. This cannot be neglected since it is comparable to the narrowest measured half-widths shown in Figure 5C. In our case there is an additional broadening contribution due to the size of the CCD pixels. An accurate calculation of the number of lamellae awaits future measurement of the time dependence of the broadening of the higher order lamellar reflections. [For a detailed discussion of instrumental and disorder broadening, see Klug and Alexander (1974)].

RESULTS

All measurements described below refer to the $L_{\beta'}/L_\alpha$ phase transition in fully hydrated DHPE. The transition temperature (T_t) at atmospheric pressure is ~68 °C and is quite sharp. As a preliminary to the kinetic experiments, static X-ray diffraction measurements were made in the vicinity of the transition region. Specifically, the pressure dependence of T_t was determined by measuring T_t in the heating direction at 0 MPa, 6.9 MPa (1000 psig), and 13.8 MPa (2000 psig). T_t was evaluated by using TRXRD and focusing on the (001) low-angle reflection, as is described in more detail below for the kinetic measurements. The sample was equilibrated for ca. 2 min at each temperature before the diffraction pattern was recorded. The operational definition of T_t is the temperature at which the relative intensities of the (001) reflection from the L_α and $L_{\beta'}$ phases are equal as judged by visual inspection of the video recorded images. The equation for the line of best fit to the three data points is $T = 68.36 + 0.16P$ ($r^2 = 0.98$) where T is given in degrees celsius and P in megapascals. From the slope of the line, a value for $\mathrm{d}P/\mathrm{d}T$ = 6.25 MPa/°C is obtained. We are not aware of a previously reported measurement of this quantity. By way of comparison, however, Utoh and Takemura (1985) have published a $\mathrm{d}P/\mathrm{d}T$ value of the order of 4.8 MPa/°C for DPPC. Sample diffraction patterns encompassing both low- and wide-angle regions from the two equilibrium phases are presented in Figure 4. The corresponding d-spacing values in the two phases and coexistence region at different equilibrium pressures and temperatures are presented in Table I.

Kinetic measurements made on a fully hydrated sample of DHPE held at a temperature just above the T_t are presented in Figures 5 and 6. Figure 5 shows the original data presented as peak intensity, peak position, and peak half-width as a function of time following the release of pressure from 9.7 MPa (1400 psig) to atmospheric pressure at t = 10 s. Also included in the figure is the change in pressure and in-sample temperature following the pressure jump.

The data show that atmospheric pressure is reached within 3 s (Figure 5E). In-sample temperature falls immediately upon the release of pressure (Figure 5D). The lowest temperature, 67 °C, is reached in ca. 1 s and is maintained for ca. 3 s. The initial temperature of 68 °C is recovered relatively slowly over the course of the next 20 s. The absorption of heat during the phase interconversion causes cooling and is the reason for the slow return to the initial temperature. Is the initial fast cooling caused by an energetic intrabilayer event not observed in the (001) reflection because it does not affect the interlamellar spacing? Not necessarily, since the expansion of residual gases and relief of stresses in seals and pipes also contribute to cooling. The definitive answer to this question depends on the measurement of the (wide-angle) intrabilayer chain-packing reflections.

The progress of the pressure-jump-induced $L_{\beta'}$ to L_α transition itself is shown in Figure 5A–C. Figure 5A shows the

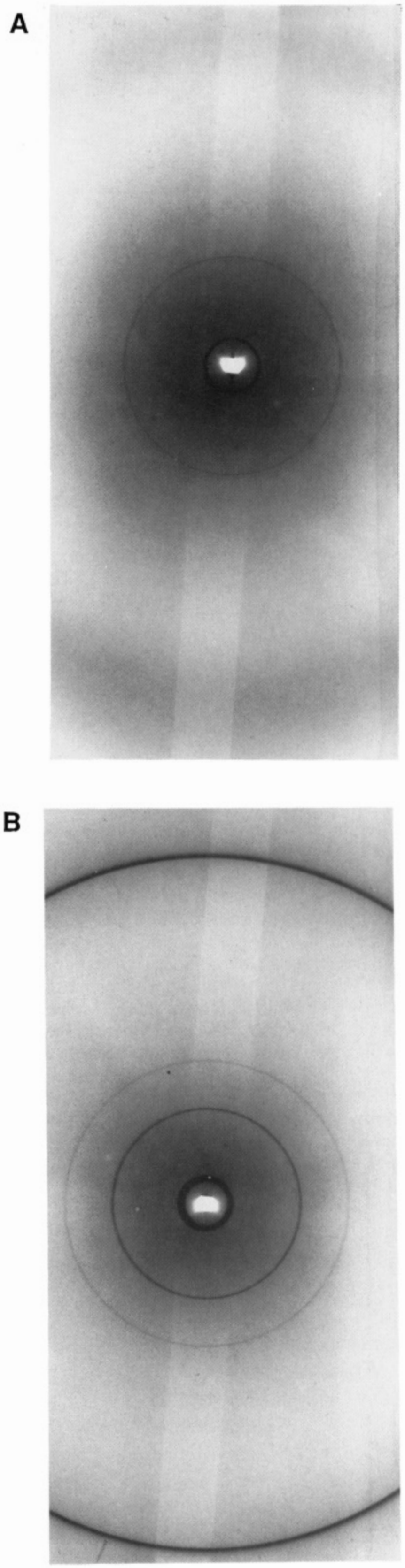

FIGURE 4: Diffraction pattern of fully hydrated DHPE recorded at 68–69 °C on X-ray sensitive film at atmospheric pressure (A) and 13.8 MPa (2000 psig) (B). In (A) the low-angle reflections are at 52.9 and 13.1 Å. The wide-angle diffuse band is centered at 4.5 Å. In (B) the low-angle reflections are at 60.6, 52.9, 15.1, and 10.1 Å. The wide-angle reflection is at 4.3 Å. Experimental conditions used in making these exposures include the following: sample-to-film distance, 120 mm; X-ray wavelength, 1.564 Å; collimator diameter, 0.3 mm; incident flux, 8×10^{10} photons/s; electron beam current, 20–60 mA; machine energy, 5.44 GeV; exposure time, 30 s.

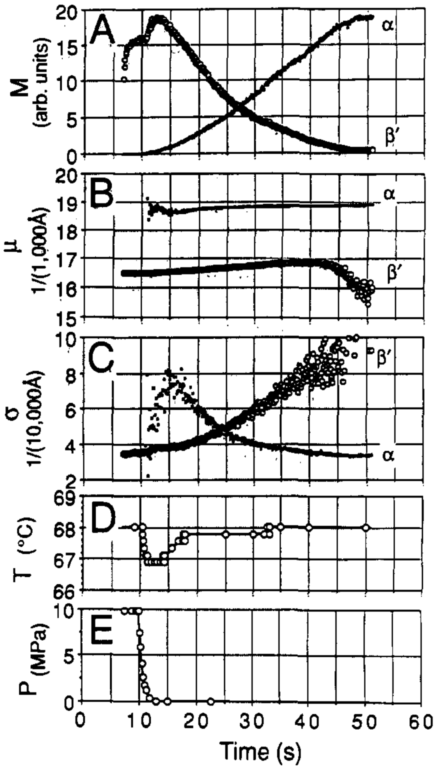

FIGURE 5: Progress of the $L_{\beta'}$ to L_α phase transition in fully hydrated DHPE induced by a pressure jump from 9.7 MPa (1400 psig) to atmospheric pressure and monitored by TRXRD. In this figure the low-angle (001) diffraction peak maximum intensity, *M*, is shown in (A) as it changes with time in the L_α (α) and $L_{\beta'}$ (β') phases during the course of the transition. The position, μ, is shown in (B). The half-width at half-height, σ, is shown in (C). The linearity of the dependence of $\mu_{\beta'}$ on time in the 12–40-s region as shown in (B) is evidenced by a line of best fit described by $\mu_{\beta'} = 161.8 + 0.1126t$ ($r^2 = 0.991$). The pressure jump is initiated at 10 s. The initial rise in intensity shown in (A) associated with the $L_{\beta'}$ phase before the pressure jump begins derives from a powering up of the intensifier/video system upon opening the X-ray shutter. The in-sample temperature, *T*, during the experiment is shown in (D), where the circles represent readings taken during the experiment from the output of an analog-to-digital converter and the line is an interpolation of these readings (see also Figure 7D). The circles shown in the time evolution of pressure, *P* (*E*), were determined in a separate measurement and were corrected for a difference in volume as described under Experimental Procedures and in the Appendix. Again the line is an interpolation between points. Panels A, B, and C contain each ca. 500 discrete time points.

peak intensity ($M_{\beta'}$) of the (001) reflection from the $L_{\beta'}$ and L_α phases as a function of time following the pressure jump initiated at 10 s. The intensity recorded at 10 s corresponds to the maximum intensity of the (001) reflection from the $L_{\beta'}$ phase in the absence of the L_α phase. Immediately following the release of pressure, $M_{\beta'}$ increases, reaching a maximum in ca. 2 s, and then slowly declines over a period of 35 s. Simultaneously, the L_α phase emerges, grows, and, with time, becomes the dominant phase. This is evidenced by a gradual, monotonic rise in M_α over a period of 35 s as the transformation takes place.

During the course of the transition the peak position (μ) of both phases shifts to slightly higher angles, corresponding to a decrease in *d* spacing. The degree of change is greatest in the case of the $L_{\beta'}$ phase. Remarkable is the linearity of the change in $\mu_{\beta'}$ with time during the first 30 s of the phase transition (Figure 5B).

Peak width for the two phases was also followed throughout the transition (Figure 5C). In both cases, peak width reaches a maximum when the phase from which it arises is the minor component. Thus, as the fraction of a given phase grows, its corresponding (001) low-angle reflection sharpens. Note also that when a given phase represents ≤5% of the total sample, it becomes increasingly difficult to fit the corresponding diffraction peak by using the nonlinear least-squares fitting procedure described under Experimental Procedures. This accounts for the spread in the data toward the beginning and end of the transition for the minor phase. For this reason, we do not attach any significance to the width data for the L_α phase below 15 s in Figure 5C.

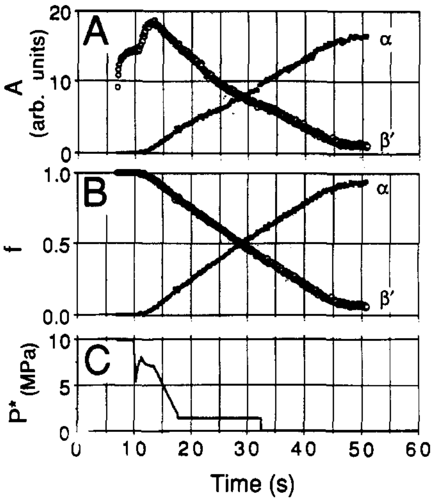

FIGURE 6: Progress of the $L_{\beta'}$ to L_α phase transition in fully hydrated DHPE induced by a pressure jump from 9.7 MPa (1400 psig) to atmospheric pressure. Presented in this figure are the quantities derived from the experimental data shown in Figure 5. Integrated diffracted intensity in the (001) low-angle peak, *A*, (peak area) from the L_α and $L_{\beta'}$ phases is shown in (A). Relative area fraction, *f*, is shown in (B). The effective pressure, P^*, during the course of the transition is included in (C) and is obtained by applying eq 7 to the interpolated points in Figure 5, panels D and E. Pressure-jump perturbation is initiated at t = 10 s. In the interval between 13 and 47 s, the linear equation $A(t) = -496.55 + 45.30t$, where $A(t)$ is the integrated area as a function of the time (t) given in seconds, provides an excellent fit to the data ($r^2 = 0.997$).

Throughout the transition, the value of the background and flat-field parameter *C* remained nearly constant, between 12 and 13% of the maximum recorded value of peak intensity $M_{\beta'}$.

As indicated under Experimental Procedures, a number of quantities can be derived from the experimental data in Figure 5. These are presented as a function of time in Figure 6. The first derived quantity is the integrated diffracted intensity associated with each phase as the transition progresses (Figure 6A). This plot shows the reciprocal relationship between the interconverting $L_{\beta'}$ and L_α phases. The plot is similar to the intensity plot in Figure 5A from which it is derived. Of particular note is the linear nature of the progress curve for the L_α phase in the region between 13 and 47 s (Figure 6A).

The fractional conversion, which is obtained by expressing instantaneous peak area of a given phase as a fraction of the combined total area of the two phases, is shown in Figure 6B. Since the peak positions and, therefore, the sampling of the structure factor of each phase remain only approximately constant, this fractional conversion is an approximate measure of the relative amounts of lipid in each phase. Notice, however, that the initial total area immediately after the pressure drop and the final total area are approximately equal (Figure 6A). Most likely, this is due to a coincidental compensation of the difference in structure factors between the $L_{\beta'}$ and L_α phases by the geometrical (Lorenz) factors, obviating the necessity of further corrections in this particular case.

It is important to notice that the temperature change due to the heat of the $L_{\beta'}/L_\alpha$ transition tends to counter the phase

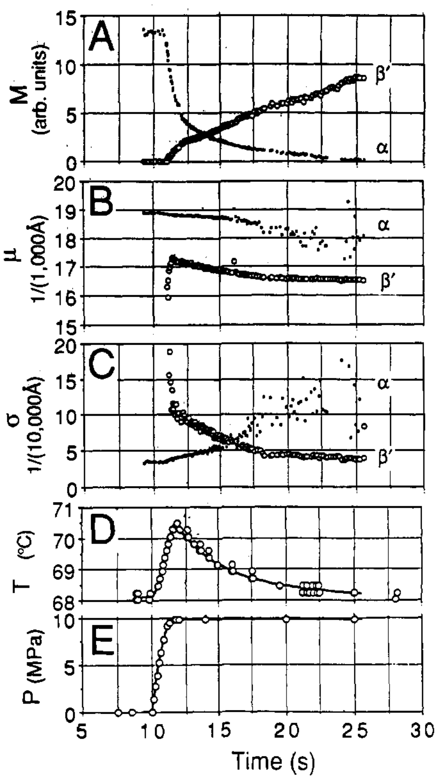

FIGURE 7: Progress of the L_α to $L_{\beta'}$ phase transition in fully hydrated DHPE induced by a pressure jump from atmospheric pressure to 9.7 MPa (1400 psig) and monitored by TRXRD. Shown in the figure are the time-dependent low-angle (001) diffraction peak maximum intensity, M (A), position, μ (B), and half-width at half-height, σ (C). The time evolution of temperature, T, is shown in (D). The dots represent experimental temperature readings as obtained from a low-resolution analog-to-digital converter; the line shows the continuous interpolation of the readings at the edge of the quantization steps. The pressure jump, P, shown in (E) was initiated at t = 10 s. The dots represent experimental readings adjusted for a volume difference, as in Figure 5E.

transition itself (LeChatelier's principle). Because of the associated temperature change, the sample is being driven through the pressure-induced phase transition region along an oblique temperature-pressure axis rather than paralleling the pressure axis. It is useful, therefore, to define an "effective pressure" P^*

$$P^* = P - \frac{\mathrm{d}P}{\mathrm{d}T}\Delta T \tag{7}$$

where the Clapeyron relation

$$\frac{\mathrm{d}P_\mathrm{t}}{\mathrm{d}T_\mathrm{t}} = \frac{\Delta H}{T\Delta V} \tag{8}$$

provides a measure of $\mathrm{d}P/\mathrm{d}T$. In determining P^* as a function of time during the transition, we have used $\mathrm{d}P/\mathrm{d}T$ = 6.25 MPa/°C obtained from the static measurements described above. The results (Figure 6C) show that P^*, in contrast to P (Figure 5E), falls at a much slower rate because of the aforementioned pressure–temperature coupling. However, we do note that P^* has dropped to zero at t = 32 s, while the transition is not complete until at least t = 45 s.

Data collected on the pressure-induced L_α to $L_{\beta'}$ phase transition are presented in Figures 7 and 8. Included in Figure 7 are the changes in (001) peak intensity, line width, and position arising from the nascent $L_{\beta'}$ and decaying L_α phases, along with pressure and in-sample temperature during the course of the transition. The derived quantities integrated intensity, relative fraction, and effective pressure are presented in Figure 8. Because of the pressure–temperature coupling during pressurization, we find that P^* rises on average at about the same rate as does phase interconversion. P^* oscillates in the beginning of the transition and becomes negative for a period. We note, however, that because the pressure development profiles in Figure 7E was determined a posteriori and not during the actual experiment there may be a slight mismatch along the time axis. Thus, we do not attach significance to the negative excursion of P^* in the 11–13-s region, although such is possible as a result of friction. Despite the ambiguity, the data suggest that the observed transition rate during pressurization is not intrinsic to the lipid sample but simply reflects the experimental limitations of achieving a fast rise to high (effective) pressures.

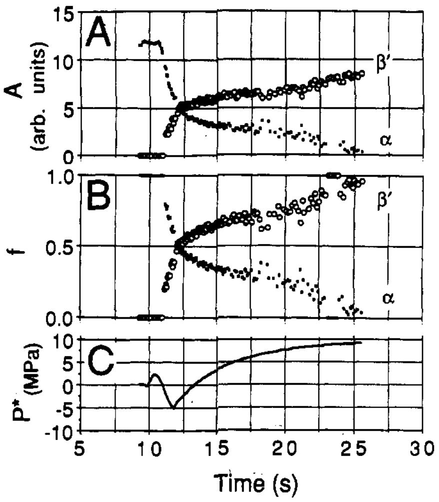

FIGURE 8: Progress of the L_α to $L_{\beta'}$ phase transition in fully hydrated DHPE induced by a pressure jump from atmospheric pressure to 9.7 MPa (1400 psig) and monitored by TRXRD. Shown in the figure are the quantities derived from the experimental data shown in Figure 7. Included in the figure are integrated intensity, A (A), relative area fraction, f (B), and effective pressure, P^* (C), as previously described in the legend to Figure 6.

We conclude that our attempts to induce a phase disequilibrium were not successful in the case of pressurization. For this reason, we emphasize depressurization, where the slow, free relaxation of the metastable state follows from an inspection and comparison of Figures 6 and 8. The *initial* drop in P^* in Figure 6C occurs on a comparable time scale as the nearly *complete* rise in P^* in Figure 8C. Since the purely geometric heat transfer characteristics are the same for the two cases, the lagging of the phase transformation behind the change in P^* in Figure 6 is due to the intrinsic slowness of the transformation. The presence of the elongated tail (beyond 18 s) in Figures 5D and 6C is associated with the absorption of heat during this slow transformation, where temperature equilibration is limited by the phase transformation and not vice versa.

DISCUSSION

By using a pressure-jump perturbation in combination with TRXRD, we have studied the dynamics and mechanism of the lamellar chain order/disorder transition in fully hydrated DHPE. By suitably adjusting temperature it was possible to induce reversibly the $L_{\beta'}/L_\alpha$ transition with a pressure jump of just 9.7 MPa (1400 psig). During pressurization the L_α to $L_{\beta'}$ transition occurs in 13 s and follows the slow loss of heat from the pressure cell. In this case, the measured transit time is limited by experimental factors and does not reflect the intrinsic value. The depressurization transition from the $L_{\beta'}$ to the L_α phase is, in contrast, significantly slower, requiring

37 s to completely transform the $L_{\beta'}$ phase. Here, the measured transit time exceeds the heat transfer characteristics of the experimental arrangement and indicates that this pressure-induced transition is intrinsically slow.

Transition Mechanism. The slow progress of the transition coupled with the linear time dependence of the conversion (f) are the features of the experimental results that most stand out. From equilibrium measurements we know that there are 10 moles of water for each mole of lipid in the L_α phase and 6 moles of water for each mole of lipid in the $L_{\beta'}$ phase (Hogan, 1989). The $L_{\beta'}$ to L_α transition requires the net uptake of 4 molecules of water per lipid molecule. We propose, therefore, that the $L_{\beta'}$ to L_α phase transition progresses at the rate water is taken up by the growing L_α phase. Since the hydration force presumably remains constant and characteristic of the new L_α phase during the transition, the rate of water uptake is also expected to be constant, and with it the rate of phase transformation. This explains the linear increase in the integrated intensity shown in Figure 6A.

Contrasting Pressurization and Depressurization. There are significant observed and interpretive differences between these two processes. Immediately obvious are the much shorter transit time, the greater heat exchange with the environment (see area under temperature vs. time plots in Figures 5D and 7D), and the greater nonlinearity associated with the pressurization when compared to the depressurization-induced transition. During pressurization 4 moles of excess water are expelled for each mole of lipid, and water loss should be faster at higher pressures. This leads to the prediction that the transit time during pressurization depends on the magnitude of the pressure jump, being shorter at higher pressure. In contrast, during depressurization to atmospheric pressure, where the transit time is controlled by viscous flow of water through and between the lipid bilayers and driven by a hydration force, no such dependence on the magnitude of the pressure jump is expected.

Simultaneous Low- and Wide-Angle Diffraction Data. Although a considerable amount of information has been extracted from the TRXRD data coupled with in-sample temperature and pressure measurements, future analysis will be enormously enhanced when a means for simultaneous low- and wide-angle diffraction data collection is implemented. In addition to allowing the separation of disorder and size effects, this will enable the monitoring of in-plane scattering changes arising from alterations in chain packing and tilt angle and the correlation of changes in long- and short-range order as the phases interconvert. It should also shed light on the possible relationship between the "chain-melting" process and the initial rapid rise in temperature.

Importance of Simultaneous Experimental Variable Measurement. Our results highlight the importance of the simultaneous measurement of as many experimental variables as possible during the course of the transition. In the present study, the evolving two-dimensional low-angle X-ray diffraction image, in-sample temperature, and elapsed time were recorded together. In the experiments presented here the pressure change was recorded separately and in-sample temperature and pressure were referenced to a common origin, viz., the point in time when the pressure jump was initiated. The jump was effected manually when the time counter reached the arbitrarily chosen value of 10 s. Thus, we estimate that the referencing of temperature and pressure to 10 s has a maximum associated error of ±1 s. Such an error would be most apparent by altering the profile of effective pressure versus elapsed time in Figures 6C and 8C. However, while the exact profile will change, our conclusions regarding the transition kinetics would not. In the depressurization direction the transition requires 37 s to complete, while the effective pressure has relaxed to nearly atmospheric within 23 s. This discrepancy strongly suggests that the pressure-induced $L_{\beta'}$ to L_α transition is intrinsically slow. In distinct contrast, the pressurization L_α to $L_{\beta'}$ transition follows the effective pressure change throughout the phase change. This suggests that the intrinsic transit time is less than the measured value of 15 s and is limited by the rate of heat transfer from the experimental apparatus to the surrounding environment.

This last conclusion could not have been arrived at without having a record of in-sample temperature during the transition. It is the effective rather than the measured pressure that is the important variable and that determines the course of the transition. In both the pressurization and depressurization transitions, the effective pressure profile is quite different from that of measured pressure. The difference arises in the time taken to reach equilibrium and in the actual profile itself. We emphasize that the exact shape of the individual profiles in Figures 6C and 8C will vary depending on how well the original temperature and pressure change profiles are aligned. Less sensitive to mismatch is the time required for effective pressure to return to equilibrium values.

Why Use a Pressure Jump? Our reasons for using the pressure jump as a trigger in the present study are many and varied. In our quest to establish the kinetics and mechanism of lipid phase transitions, to date temperature has been the trigger of choice to effect the various transformations (Caffrey, 1989a,b). The extensive use of temperature as a trigger arises because it is easy to manipulate. Temperature jump can be effected by resistance (Joule effect), laser, and microwave heating and by the use of temperature-regulated fluid (liquid and gas) streams. Each of these methods has its own set of advantages and disadvantages. The requirement in all cases is to transfer heat rapidly, uniformly and nondestructively throughout the sample. This need applies both in adjusting sample temperature from the initial to the final value and in supplying and removing the latent heat of the transition. Measurements and calculations show that heat transfer can be limiting and can result in sizable gradients and nonuniform thermal lags in the sample [see Figures 14 and 15 in Caffrey (1985)]. Thus, because of the limitations of conductive heat transfer we chose to investigate another thermodynamic trigger, pressure. Pressure has the advantage that it can be rapidly, reproducibly, and uniformly applied to a sample. It is also unlikely to bring about sample decomposition. Another important advantage is that a pressure jump can be reversed readily, thus facilitating cyclic pressure perturbation studies [see, for example, Johnson et al. (1985)]. Pressure-jump studies can be performed by using relatively inexpensive in-sample temperature sensors. The method is insensitive to sample composition and homogeneity, which are problems encountered with Joule and microwave heating. Following a pressure jump, final pressure can be maintained readily—unlike temperature during Joule and laser heating.

Temperature-jump methods in bulk samples are particularly limiting in the cooling direction. The fastest achievable cooling rate is subject to the intrinsic delays of temperature gradient driven heat conduction and dissipation processes. By comparison, in most materials pressure propagates at greater speed than temperature, such that the pressure in a bulk sample is much more rapidly responsive to active external control, making depressurization much faster than cooling. Thus, while temperature jumps tend to be slow in the downward direction, pressure jumps are potentially rapid in both the upward and downward directions.

On the negative side, the use of pressure in kinetic measurements of this sort calls for a considerable investment in the development of appropriate instrumentation and experimentation skills. There exists the need for specialized sample holders and pressure apparatus, and safety is an ongoing concern. Rapid changes in sample pressure can induce macroscopic movement of the sample in the interrogating X-ray beam and the development of bubbles upon pressure release, both of which introduce difficulties in quantitative data analysis. Correction for pressure-induced changes in sample pH must be considered also. The application of pressure deforms the sample and the pressure cell itself. Thus, there is work associated with the pressure jump that is partially dissipated as friction and partially interchanged with deformation energy and latent heat of the transition and causes the temperature of the sample to vary. Finally, the supply or removal of latent heat of the transition may, in certain cases, ultimately dictate the dynamics of the phase change.

Comparison with Other Studies. A limited number of studies have been carried out using TRXRD to study the $L_{\beta'}$ to L_α phase transition in lipid systems. For example, in the case of fully hydrated DHPE, a temperature-jump perturbation was used to induce the transition (Caffrey, 1985). In this study, a stream of temperature-regulated air flowing coaxially along the length of the sample capillary effected the order-to-disorder transition, while passive cooling in stationary air facilitated the reverse transition. It is noted also that throughout the latter measurements temperature-jump amplitude was sufficiently large that the L_α/inverted hexagonal (H_{II}) transition at ~83 °C always accompanied the lamellar order/disorder transition. The transition was found to be repeatable and reversible and to have an upper bound on the transit time of ≤3 s. The shortest recorded transit time for the chain "melting" transition was <1 s. It was also found that regardless of the direction (heating or cooling) the transition was apparently two-state to within the sensitivity limits of the TRXRD method.

Concerning the two-state nature of the transition, the pressure-jump and temperature-jump data are in agreement. At no point during the transition is there evidence for any more than the "coexisting" $L_{\beta'}$ and L_α phases. Intermediates were not observed. The big difference in the results obtained by using these two triggers arises in the recorded transit times (Table II). For both the forward and reverse pressure-induced transitions, the measured transit times are almost an order of magnitude larger than the corresponding temperature-induced changes. Does this indicate a fundamental difference between the transition brought about by temperature and pressure or is there true temperature–pressure equivalence but with the difference arising from a disparate experimental protocol? We tend to favor the latter explanation. The magnitude of the pressure jump was limited to the range of 10–13.8 MPa (1450–2000 psig). [The maximum output of the pressure regulator was 13.8 MPa (2000 psig); only rarely were the quartz capillaries used as pressure cells capable of withstanding this much pressure without bursting.] At 68 °C we found 10 MPa was just enough pressure to effect a complete phase transformation. Notice that because $dP/dT = 6.25$ MPa/°C, a pressure of 10 MPa (1450 psig) produces a deviation from equilibrium comparable to a reduction in temperature of only 1.6 °C. Thus, the driving force for the pressure-induced transition is likely to be less than that obtained in the temperature-jump study.

Table II: Characteristic Times (τ_c) of Phospholipid L_β/L_α and $L_{\beta'}/L_\alpha$ Phase Transitions Established by TRXRD

trigger		lipid	transition	τ_c (s)	reference
temperature fluid flow	↑↓	L,LD-DPPE	L_β/L_α	2	Tenchov et al. (1988)
	↑↓	DHPE	$L_{\beta'}/L_\alpha$	1–6	Caffrey (1985)
	↑↓	HOPE	L_β/L_α	2	Laggner et al. (1987)
	↑	DPPC + trehalose	L_β/L_α	2	Quinn et al. (1988)
	↑↓	L-DPPC + trehalose	L_β/L_α	2	Tenchov et al. (1988)
	↑	DMPC	$L_{\beta'}/L_\alpha$	1	Phonphok et al. (1989)
	↑	DMPC + butanol	$L_{\beta'}/L_\alpha$	4	Phonphok et al. (1989)
	↑	DMPC + octanol	$L_{\beta'}/L_\alpha$	4	Phonphok et al. (1989)
	↑	DMPC + dodecanol	$L_{\beta'}/L_\alpha$	4	Phonphok et al. (1989)
	↑	DMPC + tetradecanol	$L_{\beta'}/L_\alpha$	1	Phonphok et al. (1989)
laser	↑	SOPE	L_β/L_α	≤0.005	Kriechbaum et al. (1989)
microwave	↑↓	DHPE	$L_{\beta'}/L_\alpha$	5–10	Caffrey et al. (1990a)
pressure					
	↑	DHPE	$L_\alpha/L_{\beta'}$	13	this study
	↓	DHPE	$L_{\beta'}/L_\alpha$	37	this study

Also worthy of note is the fact that in the temperature-jump experiments final sample temperature is considerably larger (95–155 °C versus 68 °C) than was used in the pressure-jump study. Final temperature can affect transit time by changing nucleation site formation and growth rate, water viscosity, lipid permeability, and possibly other parameters (Caffrey, 1985). Thus, the pressure-jump and temperature-jump data are not directly comparable. To resolve these issues it will be necessary to conduct studies wherein final sample temperature and pressure are held constant while the rate of pressure and temperature change is varied. This will enable us to investigate the equivalence or otherwise of temperature and pressure in terms of the $L_{\beta'}/L_\alpha$ transition.

More recently, a temperature-jump TRXRD study of the $L_{\beta'}/L_\alpha$ and L_α/H_{II} transitions occurring in fully hydrated DHPE has been performed by using microwaves to effect rapid internal heating and passive cooling in air to reverse the transitions (Table II; Caffrey et al., 1990a). The results and conclusions of this study are similar to those described above for the temperature-regulated air stream measurements (Caffrey, 1985).

In the interests of completeness and to facilitate comparison, the characteristic times (τ_c) determined by TRXRD and associated data on the L_β/L_α and $L_{\beta'}/L_\alpha$ transitions are compiled in Table II. In all but one case, the τ_c values fall within the seconds to minutes range regardless of headgroup identity, acyl chain characteristics, or the presence of small molecule additives such as the disaccharide trehalose. The one exception is the SOPE system, which has a τ_c value of ≤5 ms (Kriechbaum et al., 1989). What differentiates this from the other systems is that laser heating instead of fluid flow was used to effect the temperature jump. Because these two triggers, fluid flow and laser heating, have not been compared under identical conditions, it cannot be stated with certainty that the 3 orders of magnitude difference in τ_c value derives solely from using a more rapid means to jump sample temperature. However, previous calculations and measurements have shown that fluid-flow-based temperature jumps are inherently slow because heat transfer is limited by conduction (Caffrey, 1985; Gruner, 1987).

The $L_{\beta'}$ phase has acyl chains tilted with respect to the bilayer normal. The L_β phase, in contrast, has untilted chains. Since our understanding of the mechanism of the chain order/disorder transition is still rather meager, it is not obvious whether a difference in the intrinsic rate of the transition will be observed when the L_β and $L_{\beta'}$ phases are compared.

CONCLUSIONS

We have obtained static and dynamic X-ray diffraction and temperature and pressure data on the pressure-jump-induced $L_{\beta'}/L_\alpha$ phase transition in DHPE in excess water. Upon sudden depressurization from 9.7 MPa to atmospheric pressure, the $L_{\beta'}$ to L_α transition progressed linearly with a total transit time of 37 s and a rate of phase change nearly constant over the entire transformation. The constancy of the rate of transformation, combined with the need for an uptake of 4 moles of water per mole of lipid upon transformation from $L_{\beta'}$ to L_α, suggests that the rate of this transition may be governed by (viscous) water transport driven by a constant hydration force. The experimental observation that the reverse transition, L_α to $L_{\beta'}$, induced by sudden pressurization, occurs at a rate more than 2.5 times faster than the former transition agrees with this picture, since the 4 moles of water per mole of lipid are now being expelled under the action of a high external pressure. This leads directly to the prediction that the rate of the pressure-jump-induced L_α to $L_{\beta'}$ transition will be the faster the larger the pressure jump.

Although we obtained only the time evolution of the (001) lamellar reflection, it is apparent that the large quantity of data generated by TRXRD in this experiment has proven useful in understanding the pressure-induced $L_{\beta'}$ to L_α phase transition. Nevertheless, it is clear that for a better description of the events within the bilayers higher order reflections will be required in future experiments.

ACKNOWLEDGMENTS

We thank Dr. Boris W. Batterman (National Science Foundation Grant DMR 81-12822) and the entire CHESS and MacCHESS (National Institutes of Health Grant RR-014646) staff for their invaluable help and support; Dr. Wilfred Shildkampf in particular gave valuable advice on ways to obtain high pressures. We further thank Drs. Sol M. Gruner and Allen Blaurock for critically reading the manuscript and Ms. Sharon Kraft for assistance with the typing.

APPENDIX

(*1*) *Pressure Cell and Gauge Volume Measurement.* In order to correct measurements made by using a pressure gauge in place of the pressure cell, it is necessary to know the relative internal volumes of the devices. Because of their complicated internal and external shapes and because they are heavy (ca. 200 g) compared to their internal volume, an indirect means for measuring internal volume was devised as follows. The object whose internal volume (U) is to be determined is connected at atmospheric pressure (P) by a length of Teflon tubing (internal diameter, $2r$) to an air-filled syringe. The tubing contains two small plugs of water separated from one another by a length of trapped air (m) and from the container of unknown volume by a length (n) of trapped air. The syringe is compressed, generating a pressure (P') uniformly throughout the system until the water plug next to the container is flush with it and n is reduced to zero. Under this new condition m has become m'. If temperature remains constant and expansion of the Teflon tube is negligible throughout this procedure, Boyle's law (PV = constant) can be used to solve for U as follows:

$$Pm = P'm' \tag{A1.1}$$

$$P(\pi r^2 n + U) = P'U \tag{A1.2}$$

Rearranging (A1.1) and (A1.2) gives

$$\frac{P'}{P} = \frac{m}{m'} \tag{A1.3}$$

and

$$\pi r^2 n + U = \frac{P'}{P}U \tag{A1.4}$$

Substituting (A1.3) into (A1.4) and solving for U provides

$$U = \frac{\pi r^2 n}{m/m' - 1} \tag{A1.5}$$

Thus, U is expressed in terms of the four measurable quantities r, n, m, and m'. Note that when one is interested only in the ratio of two unknown volumes it is not necessary to know either r or n.

Our measurements provide values for V_{gauge} and V_{cell} of 2.26 and 1.23 cm^3, respectively. Volume measurement error arises from error in determining water plug position, which is of order 5%. Extremely narrow tubes should be avoided in such measurements, however, because of complications arising from capillarity effects.

(*2*) *Pressure Measurement.* A reading of pressure as a function of time was obtained by attaching a constantan wire to a Bourdon tube by means of a spiral spring. The constantan wire, which has a very low temperature-resistance coefficient and which is part of a resistive bridge circuit, provides an electrical output easily recorded on a strip-chart recorder. The spring connection of the constantan wire to the Bourdon gauge guarantees that the voltage output of the bridge circuit is proportional to the pressure. In these measurements it is important to use well-annealed constantan wire of high quality. Copper and stainless steel will give erratic readings possibly due to internal stresses.

REFERENCES

Blaurock, A. E. (1982) *Biochim. Biophys. Acta 650*, 167–207.

Caffrey, M. (1984) *Nucl. Instrum. Methods 223*, 329–338.

Caffrey, M. (1985) *Biochemistry 24*, 4826–4844.

Caffrey, M. (1987) *Biochemistry 26*, 6349–6363.

Caffrey, M. (1989a) *Annu. Rev. Biophys. Biophys. Chem. 18*, 159–186.

Caffrey, M. (1989b) *Top. Curr. Chem. 151*, 75–109.

Caffrey, M., & Bilderback, D. H. (1983) *Nucl. Instrum. Methods 208*, 495–510.

Caffrey, M., & Bilderback, D. H. (1984) *Biophys. J. 45*, 627–631.

Caffrey, M., Magin, R. L., Hummel, B., & Zhang, J. (1990a) *Biophys. J. 58*, 21–29.

Caffrey, M., Fanger, G., Magin, R. L., & Zhang, J. (1990b) *Biophys. J. 58*, 677–686.

Cevc, G., & Marsh, D. (1987) in *Phospholipid Membranes: Physical Principles and Models*, Wiley-Interscience, New York.

Franks, N. P., & Levine, Y. K. (1981) in *Membrane Spectroscopy* (Grell, E., Ed.) pp 437–487, Springer-Verlang, New York.

Gruner, S. M. (1987) *Science 23*, 305–312.

Guinier, A. (1963) *X-Ray Diffraction in Crystals, Imperfect Crystals and Amorphous Bodies*, pp 123–124, 302–303, 306–309, W. H. Freeman and Co., San Francisco, CA.

Biochemistry **1991**, *30*, 2463–2470 2463

Hogan, J. L. (1989) Ph.D. Thesis, The University, Southampton, England.

Johnson, M. L., Van Osdol, W. W., & Frasier, S. G. (1985) *Comments Mol. Cell. Biophys. 3*, 77–98.

Klug, H. P., & Alexander, L. E. (1974) *X-Ray Diffraction Procedures: For Polycrystalline and Amorphous Materials*, pp 618, 634–635, J. Wiley and Sons, New York.

Kriechbaum, M., Rapp, G., Hendrix, J., & Laggner, P. (1989) *Rev. Sci. Instrum. 60*, 2541–2544.

Laggner, P., Lohner, K., & Muller, K. (1987) *Mol. Cryst. Liq. Cryst. 151*, 373–388.

Luzzati, V. (1968) in *Biological Membranes, Physical Fact and Function* (Ed. D. (Chapman, D., Ed.) pp 1, 71–123, Academic Press, New York.

Phonphok, N., Westerman, P. W., Lis, L. J., & Quinn, P. J. (1989) *J. Colloid Interface Sci. 127*, 487–491.

Quinn, P. J., Koynova, R. D., Lis, L. J., & Tenchov, B. G. (1988) *Biochim. Biophys. Acta 942*, 315–323.

Tate, M. W. (1987) Ph.D. Thesis, Princeton University, Princeton, NJ.

Tenchov, B. G., Lis, L. J., & Quinn, P. J. (1988) *Biochim. Biophys. Acta 942*, 305–314.

Utoh, S., & Takemura, T. (1985) *Jpn. J. Appl. Phys. 24*, 356–360.

Effect of Cholesterol on the Ethanol-Induced Interdigitated Gel Phase in Phosphatidylcholine: Use of Fluorophore Pyrene-Labeled Phosphatidylcholine[†]

Hiroaki Komatsu[‡] and Elizabeth S. Rowe[*]

Department of Biochemistry and Molecular Biology, University of Kansas Medical Center, Kansas City, Kansas 66103, and Veterans Administration Medical Center, Kansas City, Missouri 64128

Received June 15, 1990; Revised Manuscript Received October 12, 1990

ABSTRACT: It is now recognized that many amphiphilic molecules such as ethanol can induce the formation of the fully interdigitated gel phase ($L_\beta I$) in phosphatidylcholines (PC's). In the present study, we have developed a simple detection method for the $L_\beta I$ phase using pyrene-labeled PC (PyrPC), which is a PC analogue with a covalently coupled pyrene moiety at the end of one of its acyl chains. The intensity ratio of its fluorescence vibrational bands is a reflection of the polarity of the environment of the fluorophore. We have tested this fluorophore in several established interdigitated lipid systems, including 1,2-dipalmitoyl-*sn*-glycero-3-phosphocholine (1,2-DPPC) in the presence of high concentrations of ethanol and 1,2-di-*O*-hexadecyl-*sn*-glycero-3-phosphocholine (DHPC) and 1,3-dipalmitoyl-*sn*-glycero-2-phosphocholine (1,3-DPPC) in the absence of any additives. We have found in each of these systems that the ratio of the intensities of band III (387.5 nm) to band I (376.5 nm) is sensitive to the lipid phase change from the noninterdigitated L_β' phase to the interdigitated $L_\beta I$ phase. By comparison of the III/I ratios for PyrPC in the lipid systems with the III/I ratios for methylpyrene in organic solvents, it was shown that the polarity of the PyrPC environment in the $L_\beta I$ phase is similar to that of pentanol or ethanol. Using this method, we investigated the effect of cholesterol on the ethanol induction of the interdigitated gel phase in 1,2-DPPC. We found that the ethanol induction of the interdigitated gel phase is prevented by the presence of 20 mol % cholesterol.

It is now well established that saturated symmetrical and asymmetrical phosphatidylcholines (PC's)[1] can exist in the interdigitated gel phase ($L_\beta I$) under a variety of conditions (McDaniel et al., 1983; Serrallach et al., 1983; Huang et al., 1983; McIntosh et al., 1983, 1984; Simon & McIntosh, 1984; Hui et al., 1984; Ruocco et al., 1985; Cunningham & Lis, 1986; Hui & Huang, 1986; Mattai et al., 1987; Slater & Huang, 1988). The saturated symmetrical PC's and phosphatidylglycerols (PG's) become interdigitated in the presence of various amphiphilic molecules such as glycerol, methanol, ethylene glycol, benzyl alcohol, chlorpromazine, tetracaine (McDaniel et al., 1983; McIntosh et al., 1983), ethanol (Simon & McIntosh, 1984), and thiocyanate ion (Cunningham & Lis, 1986). Polymyxin B and myelin basic protein can also induce the formation of $L_\beta I$ in PG's (Boggs et al., 1981; Ranck & Tocanne, 1982; Boggs & Rangaraj, 1985). $L_\beta I$ has also been observed in the absence of any inducer in 1,2-dihexadecylphosphatidylcholine (DHPC) (Ruocco et al., 1985; Laggner et al., 1987; Kim et al., 1987), in 1,3-dipalmitoyl-*sn*-glycero-

---

[†] This work was supported by the Medical Research Service of the Department of Veterans Affairs and by a grant from the National Institute of Alcohol Abuse and Alcoholism (AA 05371).

[*] Address correspondence to this author at Research Services, Veterans Administration Medical Center, 4801 Linwood Blvd., Kansas City, MO 64128.

[‡] Present address: Faculty of Pharmaceutical Sciences, Kyoto University, Yoshida-shimoadachi, Sakyo-ku, Kyoto 606, Japan.

[1] Abbreviations: PC, phosphatidylcholine; PG, phosphatidylglycerol; 1,2-DPPC, 1,2-dipalmitoyl-*sn*-glycero-3-phosphocholine; 1,3-DPPC, 1,3-dipalmitoyl-*sn*-glycero-2-phosphocholine; 1,2-DSPC, 1,2-distearoyl-*sn*-glycero-3-phosphocholine; DHPC, 1,2-di-*O*-hexadecyl-*sn*-glycero-3-phosphocholine; PyrPC, 1-palmitoyl-2-pyrenedecanoyl-*sn*-glycero-3-phosphocholine; MePyr, 1-methylpyrene; DPH, 1,6-diphenyl-1,3,5-hexatriene; Tris, tris(hydroxymethyl)aminomethane; EDTA, disodium ethylenediaminetetraacetate; L_c, crystalline subgel bilayer phase; L_β', tilted-chain bilayer gel phase; P_β', rippled gel phase; L_α, liquid-crystalline bilayer phase; $L_\beta I$, interdigitated gel phase; DSC, differential scanning calorimetry.

0006-2960/91/0430-2463$02.50/0